The influences of corrosion degree and uniformity on bond strength and cracking pattern of cement mortar and PVA-ECC

Chuanqing Fu[1,*]; Rui He[2]; Kejin Wang[3,*]

1. College of Civil Engineering, Zhejiang University of Technology, Hangzhou, 310023, China, chqfu@zjut.edu.cn (*corresponding author)
2. College of Civil Engineering and Architecture, Zhejiang University, Hangzhou 310027, P.R.China, henry-hr@zju.edu.cn
3. Department of Civil, Construction and Environmental Engineering, Iowa State University, Ames, IA, 50010, USA, kejinw@iastate.edu (*corresponding author)

Abstract: Engineered Cementitious Composite (ECC), which has a strain-hardening behavior under tension, has been widely used for repairing and retrofitting the reinforced concrete structures. In such applications, the performance of the bonding between the ECC and corroded rebar is critical for the service life prediction of the repaired structures. In this work, the cracking patterns and bond behavior of polyvinyl alcohol engineered cementitious composites ECC (PVA-ECC) and cement mortar with uniform and non-uniform corroded steel rebars were studied. It is found that the uniform corrosion induced cracks were randomly distributed while the non-uniform corrosion induced cracks would concentrate perpendicular to most corroded side. The bond strength of PVA-ECC and mortar specimens is independent with corrosion method. The bond strength of PVA-ECC and mortar specimens both showed a trend of increasing first and then decreasing with the development of corrosion rate. The threshold corrosion rate for mortar specimen is 0.125% while the PVA-ECC specimen has the threshold corrosion rate value of 0.922%.

Key words: Uniform corrosion; Non-uniform corrosion; Polyvinyl Alcohol Engineered Cementitious Composite (PVA-ECC); Cracking pattern; Bond strength

1. Introduction

1.1. Research background

The corrosion of steel reinforcements in concrete is a long-standing problem (He et al. 2019; Li et al. 2008) for the durability performance of reinforced concrete (RC). Corrosion of reinforcing bar (rebar) can cause widespread damage to RC structures, including the reduction of the rebar cross section, and weakening the concrete-rebar bond strength. Moreover, the generated cracks on concrete surface can provide more transport path for contamination mass (Fu et al. 2022; He et al. 2018, 2022), which might cause further corrosion. Thus, the studies of cracking distribution and bond strength deterioration of corroded RC structures are of great importance for durability prediction and repairing of the cracked structures.

1.2. Bond behavior

Upon the propagation of rebar corrosion, the reduction of cross-sectional area of steel rebar and the generated cracks in concrete cover could lead to the degradation of bond performance (Abosrra et al. 2011; He et al. 2020; Lin et al. 2019; Okada et al. 1988; Stewart 2009). The bond consists of three aspects, which are, chemical adhesion, friction and mechanical interlock in between concrete and rebar. At low pull-out stress level, the bond strength is mainly determined by the chemical adhesion. Many studies have proved that, during this period, the bond strength is provided by the compressive strength of the surrounding concrete (AL-mahmoud et al. 2007; Zhu et al. 2018b). Once the slip occurs, chemical adhesion disappears, and the bond is assured by the friction and mechanical interlock (Fu et al. 2021; Zhu et al. 2018a). During this period, the tensile strength of the surrounding concrete plays a dominate role in determining the bond strength (Ju et al. 2020).

Extensive research has been dedicated to understanding the bond behavior of corroded RC structures. Lee et al. (Lee et al. 2002) found that before the cracking of concrete cover, the bond strength of corroded RC structure was higher than that of the plain RC structure. Fang et al. (Fang et al. 2006) revealed that for confined RC structures, a medium corrosion level (at around 4%) had no substantial influence on the bond strength while a significant reduction in bond strength was observed when the corrosion degree exceeded 6%. Tondolo (Fang et al. 2006) found the critical corrosion level for bond strength reduction was 2%. Zhu et al. (Zhu et al. 2018a) investigated the bond strength of non-uniformly corroded RC structures and found the bond strength reached peak when the corrosion degree was 0.25-0.3%. Huang (Huang 2014) found that for uniformly corroded steel rebar, the critical corrosion level for bond strength increase was 3%. Coccia et al. (Coccia et al. 2016) found that for plain round steel rebar, the corrosion degree of 0.5-0.6% was the critical value to reach the peak bond strength.

It can be found that the low corrosion degree leads to the increase of bond strength while a further increase in corrosion level could result in a significant reduction in bond strength. However, the critical corrosion level is influenced by corrosion uniformity, steel types (i.e., plain round steel and threaded steel) and the surrounding cementitious material types.

1.3. Corrosion cracking pattern

In addition to the bond behavior, cracking pattern is also of great importance in durability study of RC structures. The generated corrosion cracks lead to the release of ring stress of steel rebar which could result in the reduction of the bond strength (Fu et al. 2021; Zhang et al. 2009). Moreover, cracks provide more path for the transport of aggressive mass which could significantly increase the corrosion rate of reinforcement (Fu et al. 2017; Zhu et al. 2018b). Thus, the study of cracking patterns of corrosion RC structures could provide evidence for repair of corroded RC structures.

However, few literatures focus on the evolution of corrosion induced cracking patterns, not to mention the influence of corrosion uniformity, cementitious matrix type and corrosion degree on the development of cracking pattern. It was found that corrosion uniformity plays an important role in distribution of cracking patterns due to the stress concentration of non-uniform corrosion (Fu et al. 2021). Zhang et al. (Zhang et al. 2009) studied the influence of cracking pattern on the serviceability of RC concrete beam. It was found that under non-uniform corrosion condition, the distribution of cracks significantly influences bond degradation of RC beam and cross-section loss of the reinforcement. Yang et al. (Yang et al. 2019) found the presence of corrosion cracks obviously has a negative effect on the bond performance of RC structures. Moreover, the crack patterns were found to be more dominant than rust and rebar shape in bond deterioration mechanism. Qiao et al. (Qiao et al. 2016) found the internal crack propagation is dependent on the corrosion uniformity rather than the cover thickness.

Previous studies indicate that the corrosion cracking patterns play an essential role in bond behavior, durability performance of RC structure, while the corrosion uniformity influences the cracking patterns. However, there is still a lack of study on the effect of corrosion degree on the cracking pattern development. Thus, the study of corrosion uniformity on the influence of cracking patterns can provide a good indication in durability evaluation of RC structures.

1.4. Research Objectives

To this end, with the motivation to study the influences of corrosion degree and uniformity on bond strength and cracking pattern, this study used a recently proposed non-uniform electrochemical acceleration corrosion method to study the cracking pattern and the bonding performance of cement mortar and Polyvinyl Alcohol Engineered Cementitious Composite (PVA-ECC) materials. The critical corrosion degrees on the bond strength degradation under different corrosion uniformity conditions were analyzed. The crack width and the distributions of cracks under uniform and non-uniform corrosion conditions were studied. It is worth noting that there are a number of different varieties of ECC (i.e., lightweight ECC, self-compacting ECC, steel-fiber ECC), the research conclusion in this study may vary with the type of ECC.

2. Experimental program

2.1. Materials and mix proportion

The matrix material used in this study was composed of cement, fly ash (FA), silica sand (SS) and superplasticizer (SP). Table 1 presents the chemical compositions of Portland cement and fly ash. The cement was Type I Portland cement in compliance with ASTM C 150 (ASTM C150 / C150M-20 2020) with a specific gravity of 3.15 and fineness of 384 m^2/kg. The Class C fly ash (FA) in compliance with ASTM C618 (ASTM C618 - 19 2019) had a specific gravity of 2.52 and fineness of 419.6 m^2/kg. Silica sand (SS) with a specific gravity of 2.61 and particle sizes ranging from 180 to 270 μm was used. A very small amount of AVDA 105 superplasticizer (SP) produced by Grace Construction Products Inc. was added to adjust the rheological properties of the fresh mix for better fiber distribution and workability. The discontinuous K-II REC15 PVA fibers were manufactured by Kuraray Co., Ltd, with the physical properties indicated in Table 2.

The mix proportions of cement mortar and PVA-ECC are listed in Table 3. It shall be noted that the mix proportions of PVA-ECC and mortar are the same, except that PVA-ECC mixture had 2% (by vol. of concrete) PVA fiber, while the mortar did not.

2.2. Sample preparation

2.2.1. Mechanical test sample preparation

Three 50 mm (2 in.) cubic mortar and ECC samples, respectively, were prepared for compressive strength tests. Two dog-bone shape mortar and ECC samples, respectively, were also prepared for tensile strength tests, the shape and dimensions of tensile strength test sample were presented in Fig. 2 (a).

In this work, all specimens (including cylinder specimens discussed in following sections) were demolded at 1d age after casting and then cured in 23 °C with the relatively humidity (RH) of 95% for 28 days.

2.2.2. Corrosion uniformity sample preparation

In order to simulate the natural non-uniform corrosion condition, an electrochemical acceleration corrosion method based on the impressed current method was proposed recently in a companion work (Fu et al. 2018). Two cylindrical ECC specimens with the diameter of 100 mm (4 in.) and the height of 200 mm (8 in.) were prepared for corrosion uniformity test. The round steel rebars with the diameter of 12.7 mm (0.5 in.) and the length of 250 mm (10 in.) were embedded in the center of the cylinder specimens, respectively. A stainless-steel wire with the diameter of 0.7 mm (0.028 in.) and the length of 250 mm (10 in.) was embedded into one of the specimens for the induction of non-uniform corrosion, the distance between the surface of steel rebar and stainless wire was 5 mm (0.2 in.). The non-uniform corrosion specimen was denoted as NU and the uniform corrosion specimen was denoted as U as presented in Table 4.

The purpose of implementing cylindrical specimens was to ensure that the cover thickness was uniformly around the circumference of steel rebar. The reason of using plain round steel rebars instead of corrugated black steel rebar was to simplify the rust thickness quantification. However, it is worth noting that the applicability and effectiveness of the proposed method are independent of the morphology of steel rebar surface as well as the geometry and the size of specimen.

2.2.3. Accelerated corrosion sample preparation

36 specimens with a diameter of 150 mm (6 in.) and height of 150 mm (6 in.) were prepared to study the cracking pattern and the bonding property between the cementitious matrix and the corroded steel rebar. Round steel rebar with the diameter of 12.7 mm (0.5 in.) and the length of 575 mm (23 in.) was embedded in the center of cylinder specimen. Steel rebar was divided into 4 sections with the length of 400 mm (16 in.), 75 mm (3 in.), 75 mm (3 in.), and 25 mm (1 in.), respectively. The first (400 mm) and the last (25 mm) sections were out of specimens. The middle two sections (75 mm) were embedded into cementitious matrix. In this work, the binding length of the rebar was 75 mm. Thus, one of the embedded sections (75 mm) were separated from cementitious matrix by a PVC pipe as presented in Fig. 1 (b). These 36 cylinders specimens were divided into 4 groups. the first 2 group specimens were cast by ECC and the other 2 group specimens were cast by mortar. One of the ECC groups specimens were prepared for non-uniform corrosion with 8 specimens and denoted as NUECC, and the other group of ECC specimens were prepared for uniform corrosion with 10 specimens and denoted as UECC. The mortar group also includs with 8 non-uniform corrosion specimens denoted as NUM, and 10 uniform corrosion specimens denoted as UM. A summary of cylinder samples used in this study was concluded in Table 4.

For non-uniform corrosion specimens, stainless steel wires with the diameter of 0.7 mm (0.028 in.) and the length of 200 mm (8 in.) were embedded into cementitious matrix parallel to rebar, the distance between the surface of the rebars and stainless wires was 5 mm (0.2 in.). The configuration of the designed cylinders is shown in Fig. 1.

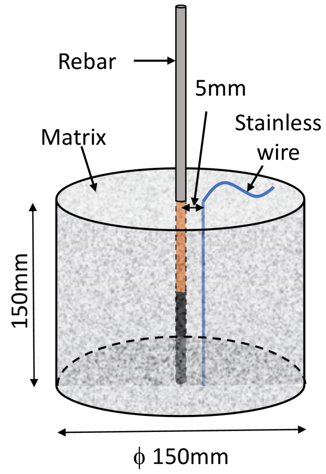

(a) Configuration of the non-uniform corrosion specimens for crack mode and bonding property study (uniform corrosion specimens did not include the stainless wire).

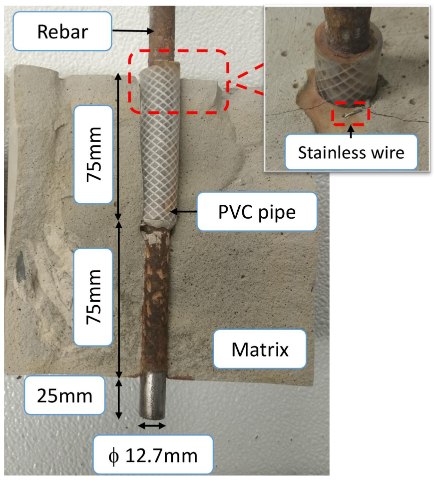

(b) Picture of the non-uniform corrosion cylinder specimens (uniform corrosion specimens did not have stainless wire).

Fig. 1. The configuration of the designed cylinders.

2.3. Test methods

2.3.1. Mechanical tests

The cracking resistance of mortar and ECC specimens in this work was mostly provided by tensile strength of the composites rather than compressive strength. Thus, at the designated age, uniaxial tension tests on dog-bone shape specimens were conducted under a displacement control condition by a mechanical testing system (MTS) testing machine, at a rate of 0.5 mm/min. Dog-bone shape specimen was widely used to determine the tensile strength of cement mortar and ECC materials (Yu et al. 2015, 2020; Zhang and Zhang 2018). Two linear variable differential transformers (LVDTs) were installed on each side of the tested specimen to measure the displacements between two points on the specimen in a gauge length of 80 mm as shown in Fig. 2 (b). Based on the recorded load (by MTS) and average displacement data (by LVDTs), the tensile stress-strain curve of the tested specimens was plotted. The compressive strength tests on cubic specimens were also performed in accordance with ASTM C109 (ASTM C109 / C109M - 20b 2020).

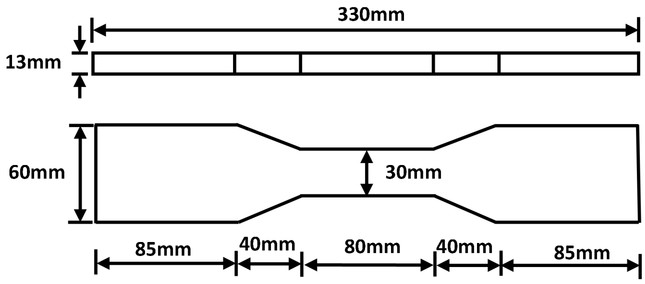

(a) Shape and dimensions of tensile strength test specimen.

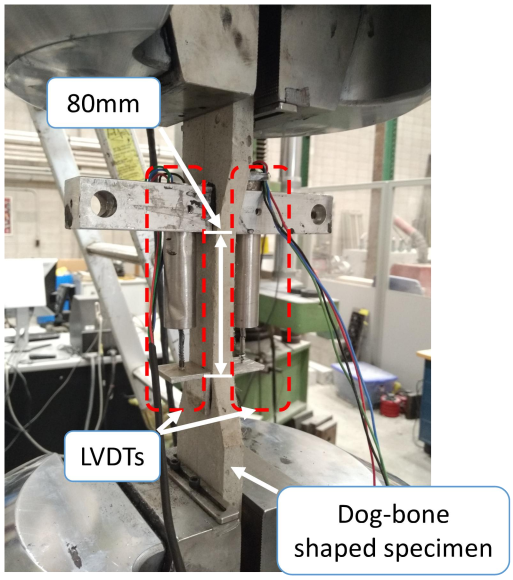

(b) Tensile strength test setup.

Fig. 2. Tensile strength test setup and specimen.

2.3.2. Accelerated corrosion uniformity tests

At the designated age, the corrosion of steel rebars in UC and NUC specimens was induced and accelerated by the impressed current method. For uniform corrosion specimen, the sample surface was wrapped with a layer of sponge saturated with 3.5% (by mass) NaCl solution, then a layer of stainless-steel mesh was wrapped on the surface of the sponge as shown in Fig. 3 (a) and (b). The reason of using saturated sponge and stainless-steel mesh is to uniformly apply the impressed current into the specimen. During the corrosion process, the stainless-steel mesh was connected to cathode while the steel rebar was connected to anode. For non-uniform corrosion sample, the steel rebar was connected to anode and the steel wire was connected to cathode as presented in Fig. 3 (c) and (d). During corrosion acceleration process, the UC and NUC specimens were connected in series and the steel rebars were connected into the anode, stainless wire for NUC specimen and stainless mesh for UC specimen were connected into the cathode of direct current (DC) power. The corrosion current density was controlled as 200 μA/cm^2 and the corrosion duration was 5 days. It is worth noting that the accelerated corrosion current density for lab study has a very wide selection. Some study used the accelerated corrosion current density higher than 1000 μA/cm^2 (Dong et al. 2017; Du et al. 2017), most of studies used the corrosion current density in a range of 100-600 μA/cm^2 for corrosion acceleration study (Fu et al. 2018; González et al. 2004; Hong et al. 2020).

After corrosion acceleration, disc samples were cut from the middle portion of NUC and UC specimens and then polished. The rust distribution and rust layer thickness of steel rebars in non-uniform and uniform corrosions were then analyzed from backscattered electron images (BSEM) obtained by a FEI QUNTA 650 environmental scanning electron microscope.

2.3.3. Uniform and non-uniform corrosion acceleration

After curing, the corrosion propagation of steel rebar in ECC and mortar cylinder specimens was accelerated by the impressed current method as shown in Fig. 3. For uniform corrosion acceleration, the surface of the specimens was wrapped with a sponge saturated with 3.5% (by mass) NaCl solution. A layer of stainless-steel mesh was then wrapped the saturated sponge. The width of the sponge and mesh was 75 mm which is the same with the corrosion section length of rebar as shown in Fig. 1. The stainless mesh and stainless wire were connected to the cathode of the DC power, respectively, for uniform corrosion and non-uniform corrosion, while the rebar was connected to the anode of the DC power. The corrosion current density for uniform corrosion and non-uniform corrosion was controlled as 200 μA/cm^2.

The 36 cylinder specimens for corrosion crack monitoring and bonding strength test were divided into 4 groups as presented in section 2.2.3. The ECC specimens for uniform (UECC) and non-uniform (NUECC) corrosion acceleration included 4 corrosion durations, which were 1 d, 2 d, 4 d and 6 d. While the uniform (UM) and non-uniform (NUM) corrosion acceleration of mortar specimens had 4 different corrosion durations, which were 8 h, 16 h, 24 h and 32 h. 2 duplicates for ECC and mortar cylinders were prepared, respectively, as reference specimens without corrosion process (i.e., UECC0 and UM0 in Table 4). Each corrosion duration specimens had 2 duplicates. The details of all cylinder specimens for corrosion acceleration were concluded in Table 4. The design corrosion rate (ρ_0) was calculated in accordance with ASTM G102 (ASTM G102-89(2015)e1 2015) and also presented in Table 4.

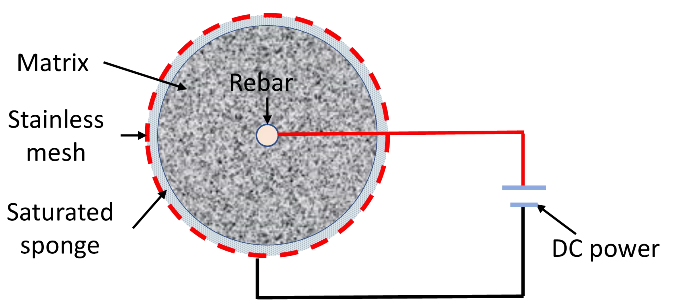

(a) Schematic for uniform corrosion acceleration.

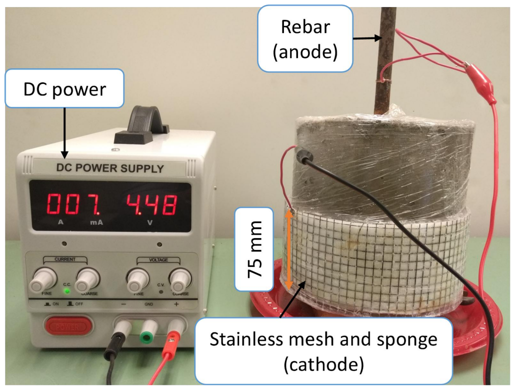

(b) Test setup for uniform corrosion acceleration.

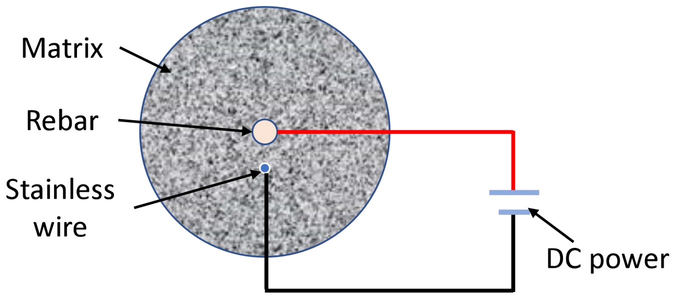

(c) Schematic for non-uniform corrosion acceleration.

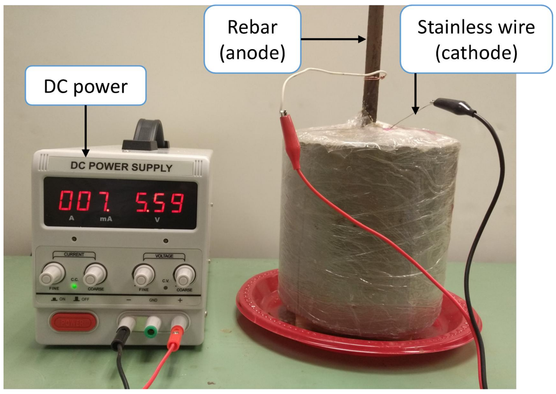

(d) Test setup for non-uniform corrosion acceleration.

Fig. 3. Test setups and schematics for uniform and non-uniform corrosion acceleration of cylinder specimens.

2.3.4. Pull-out test

After corrosion acceleration, steel rebars in cylinder specimens were pulled out by an MTS machine as illustrated in Fig. 4. The pull-out test is widely used in literature (AL-mahmoud et al. 2007; Fu et al. 2021; Li and Yuan 2013). This test has also been standardized by British Standards Institution (BS EN 12504-3 2005). The displacements of top and bottom ends of the steel rebar were recorded by two LVDT sensors and the strain of the rebar during pullout test was measured by a strain gauge. The loading speed of pullout test was 0.1 mm/min. Based on the recorded strain (by strain gauge) and average displacement data (by LVDTs), the bond stress-slip curve of the tested specimens was plotted.

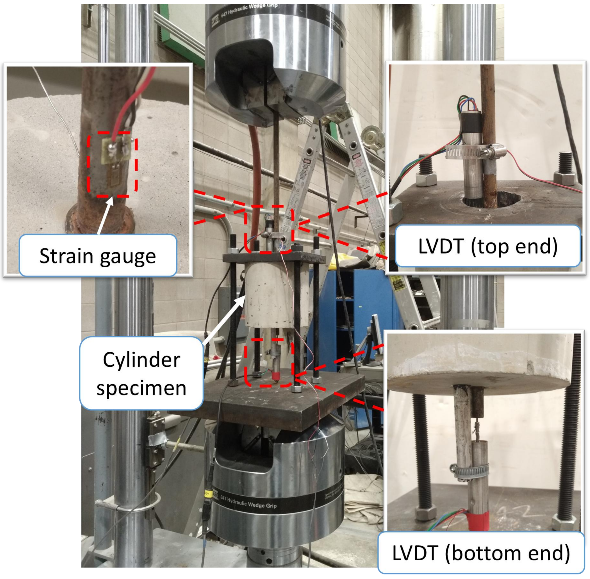

Fig. 4. Pullout test setup.

2.3.5. Crack profile recording

The position and width of cracks in cylinder specimens after corrosion acceleration and pullout test were recorded as shown in Fig. 5. The crack width was recorded by a crack visualizer with an accuracy of 0.001 mm. The crack distributions were recorded by a round plastic scale as presented in Fig. 5 (a). The plastic scale was evenly divided into 16 parts with 22.5° of each part to record the position of cracks. Red color curves in Fig. 5 (b) denote cracks induced by corrosion acceleration while blue color curves represent the crack profile after pullout test. The crack widths were measured by a crack width tester. It is worth noting that some cracks induced by corrosion acceleration might widen during the pullout test. Thus, the crack widths were measured after corrosion acceleration and pullout test, respectively.

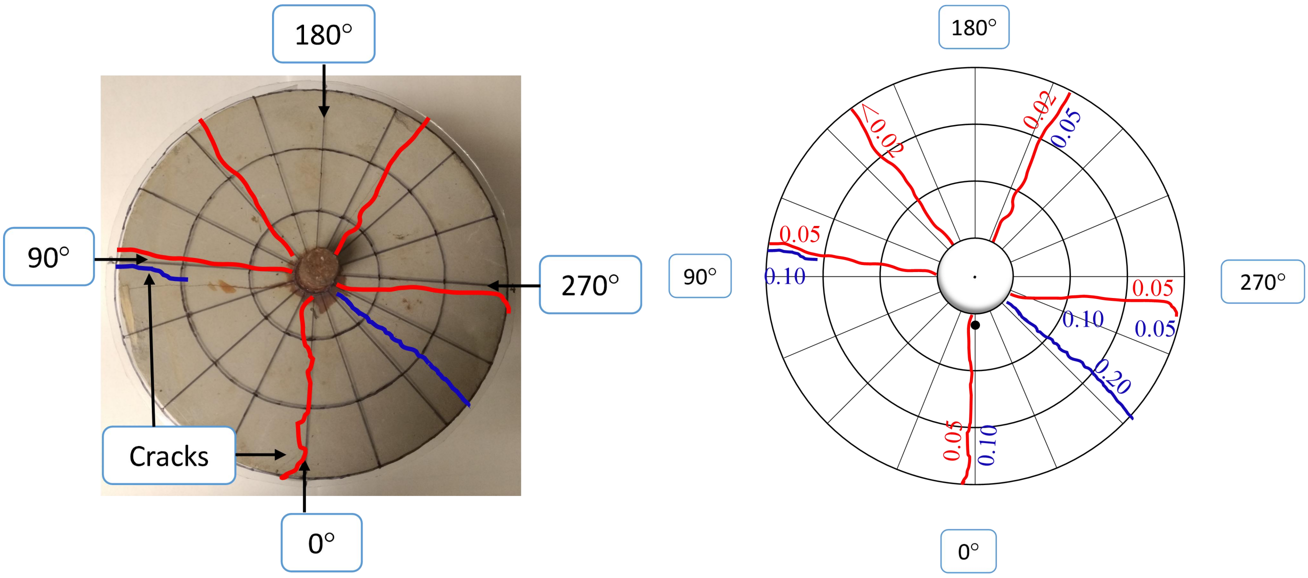

(a) Plastic film scale. (b) Crack distribution profile.

Fig. 5. Crack profile recording of cylinder specimens (red curves and numbers denote crack position and width after corrosion acceleration, blue curves and numbers denote crack position and width after pullout test).

2.3.6. Steel rebar corrosion rate determination

6 plain steel rebars with the length about 65 mm were prepared for corrosion rate calibration. Each rebar's length was measured for 3 times and the average length of each rebar was recorded. The mass of each rebar was also measured. The mass of rebar per unit length was determined and taking as average for 6 rebars (K_a).

After pullout tests, the cylinder specimens were split and corroded rebars were taken out for corrosion rate determination. Then, the corrosion section was cut from the middle portion with a length about 65 mm, and the corrosion rate was determined by weight loss method in accordance with ASTM G 103 (ASTM G1-03e1 2017). Consequently, the length of each rebar was measured for 3 times and the mass of corroded rebar after processing was determined. The mass per unit length of each corroded rebar were calculated as K_b. The corrosion rate of steel rebar was determined as:

$$\rho = \frac{K_a - K_b}{K_a} \times 100\% \tag{1}$$

where ρ (%) denotes the corrosion rate of steel rebar.

3. Corrosion uniformity simulation

Finite element method (FEM) simulations were performed to investigate the current density distribution during corrosion acceleration. Rust thickness and distribution of uniform corrosion and non-uniform corrosion were also studied by FEM method in this work. The FEM simulation was conducted using the commercial software Comsol Multiphysics®. The model geometries are shown in Fig. 6, which is comprised of a large circle with the diameter of 150 mm represents the electrolyte (ECC), a middle circle with a diameter of 12.7 mm in the center of the large circle represents the rebar. For non-uniform corrosion simulation model, a small circle with the diameter of 0.7 mm represents the stainless wire, the distance between the center of stainless wire and the surface of rebar was 5 mm. The parameters used for simulation are concluded in Table 5.

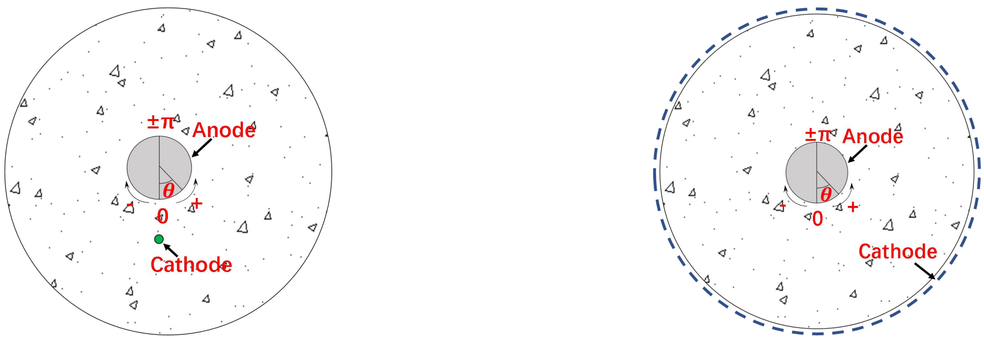

(a) Non-uniform corrosion model. (b) Uniform corrosion model

Fig. 6. Model geometries of uniform and non-uniform corrosion models (anode was steel rebar and cathode for non-uniform simulation was wire while for uniform corrosion simulation was sponge).

4. Results and discussion

4.1. Mechanical performance

The compressive strengths of ECC and mortar samples were 44.0 MPa and 45.0 MPa, respectively. The stress-strain curves of dog-bone specimens for ECC and mortar mixtures are presented in Fig. 7. What can be clearly seen from this figure is that the ECC specimens showed upgraded tensile strength and strain rate compared with mortar specimens. The tensile strengths of 2 ECC specimens were 0.85 MPa and 0.86 MPa, respectively, while the mortar specimens were 0.51 MPa and 0.54 MPa, respectively. The ultimate strain rates of ECC specimens were 2.33% and 1.63%, respectively, while the mortar specimens were 0.22% and 0.17%, respectively. The enhanced tensile strength and the strain rate of ECC specimens meet the characteristics of ECC materials (Lim and Li 1997; Ling et al. 2019), which is, the addition of PVA fiber in ECC bridges the generated cracks and significantly enhances the load and displacement capacities.

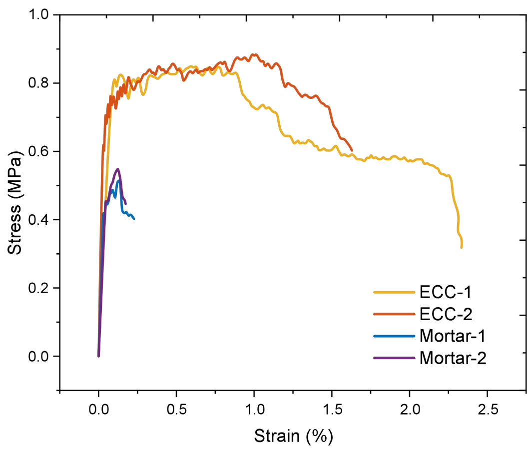

Fig. 7. Stress strain curves of dog-bone specimens.

4.2. Corrosion uniformity comparison between corrosion test and simulation results

The corrosion current density distributions of uniform and non-uniform corrosion simulation are presented in Fig. 8. Fig. 8 (a) shows that the corrosion current in the non-uniform corrosion simulation was mostly concentrated around the steel rebar on the side near the cathode (i.e., steel wire), while on the side facing away from the cathode, the corrosion current density was low. Fig. 8 (b) reveals that the corrosion current density was uniformly distributed in the uniform corrosion simulation model.

(a) Non-uniform corrosion (b) Uniform corrosion

Fig. 8. Corrosion current density distribution simulation results.

The measurement results of rust thickness distribution from BSEM tests are presented in Fig. 9. As seen in Fig. 9 (a), the rust of non-uniform corrosion sample accumulated on the side near the steel wire (cathode) while the other side had limited rust accumulated. Fig. 9 (b) reveals that the uniform corrosion sample rust was evenly distributed around the steel rebar. Fig. 9 (a) shows that the rust thickness of non-uniform corroded sample facing the cathode side was about 95 μm, while the side facing away the cathode was about 5 to 10 μm. The rust thickness of uniform corroded sample in Fig. 9 (b) was about 70 μm.

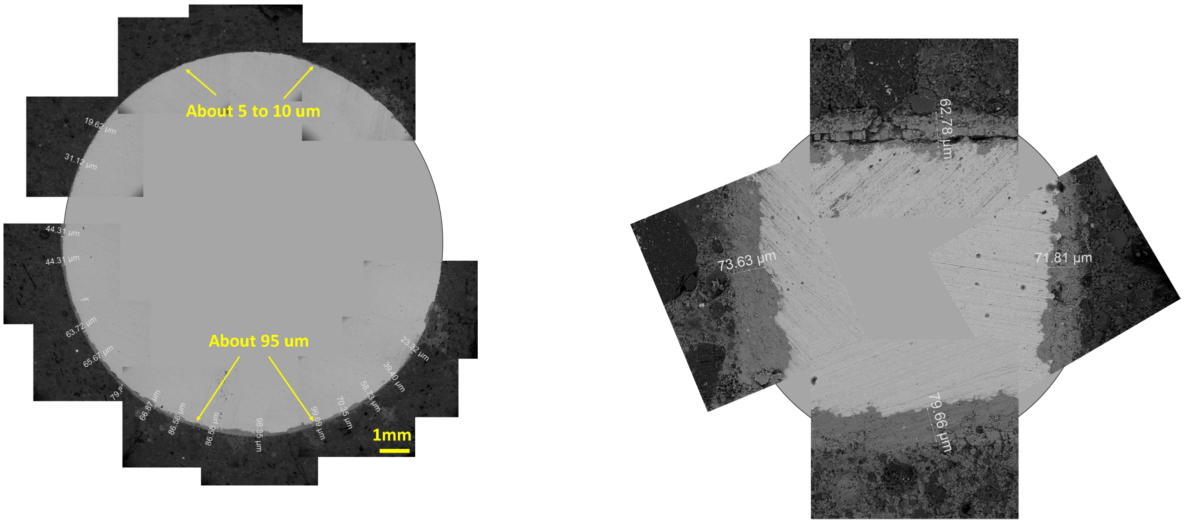

(a) Non-uniform corrosion (NUC) (b) Uniform corrosion (UC)

Fig. 9. BSEM results of rust thickness.

The rust thickness distributions of uniform and non-uniform corrosion from experiment and simulation results are presented in Fig. 10. A typical Gaussian distribution characteristic for the corrosion products can be obtained for the non-uniform corrosion sample; A similar rust distribution on non-uniform corrosion samples has been observed in Ref. (Fu et al. 2018). For the uniform corrosion sample, the distribution of the corrosion products distributed uniformly.

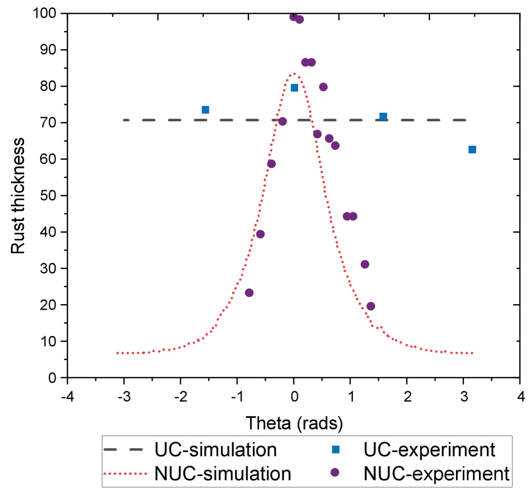

Fig. 10. Rust thickness distributions of uniform and non-uniform corrosion results from simulation and experiment.

4.3. Cracking pattern analysis

4.3.1. Cracking profiles of mortar specimens

Fig. 11 illustrates part of cracking profiles of mortar specimens subjected to uniform (UM) and non-uniform corrosion (NUM) methods, where the red curves denote the cracks induced by corrosion before the rebar was pulled out, and the blue curves are cracks recorded after the rebar pull-out test. The cracking profiles of all samples can be found in the supplementary file.

When corrosion duration was 8h (which denotes the design corrosion rate, ρ_0, was 0.05% as presented in Table 4), no corrosion crack was observed in NUM and UM samples. When corrosion duration increased to 16h (ρ_0=0.11%), corrosion cracks were observed in NUM samples and in UM samples. In NUM samples, the average crack width at 16h was 0.08 mm; In the UM samples, it was 0.02 mm. With the development of corrosion duration, the crack numbers increased, and crack width of each sample was more pronounced. The NUM samples always showed larger corrosion cracks than UM samples (i.e., at 32h corrosion duration, the average crack widths for NUM and UM samples were 0.15 mm and 0.05 mm, respectively). This could result from the accumulation of rust in one side of NUM that caused the stress concentration. In the case of uniform corrosion, the corrosion products were evenly distributed around the steel rebar, as indicated in Fig. 9. Thus, with the same design corrosion rate, the stress generated by the corrosion products of uniform corroded samples was lower thasn non-uniform corroded samples. After the pull-out test, the pull-out cracks (blue curves in Fig. 11) developed along the location of the main corrosion crack (red line). With longer corrosion time, the width of the pull-out crack increased.

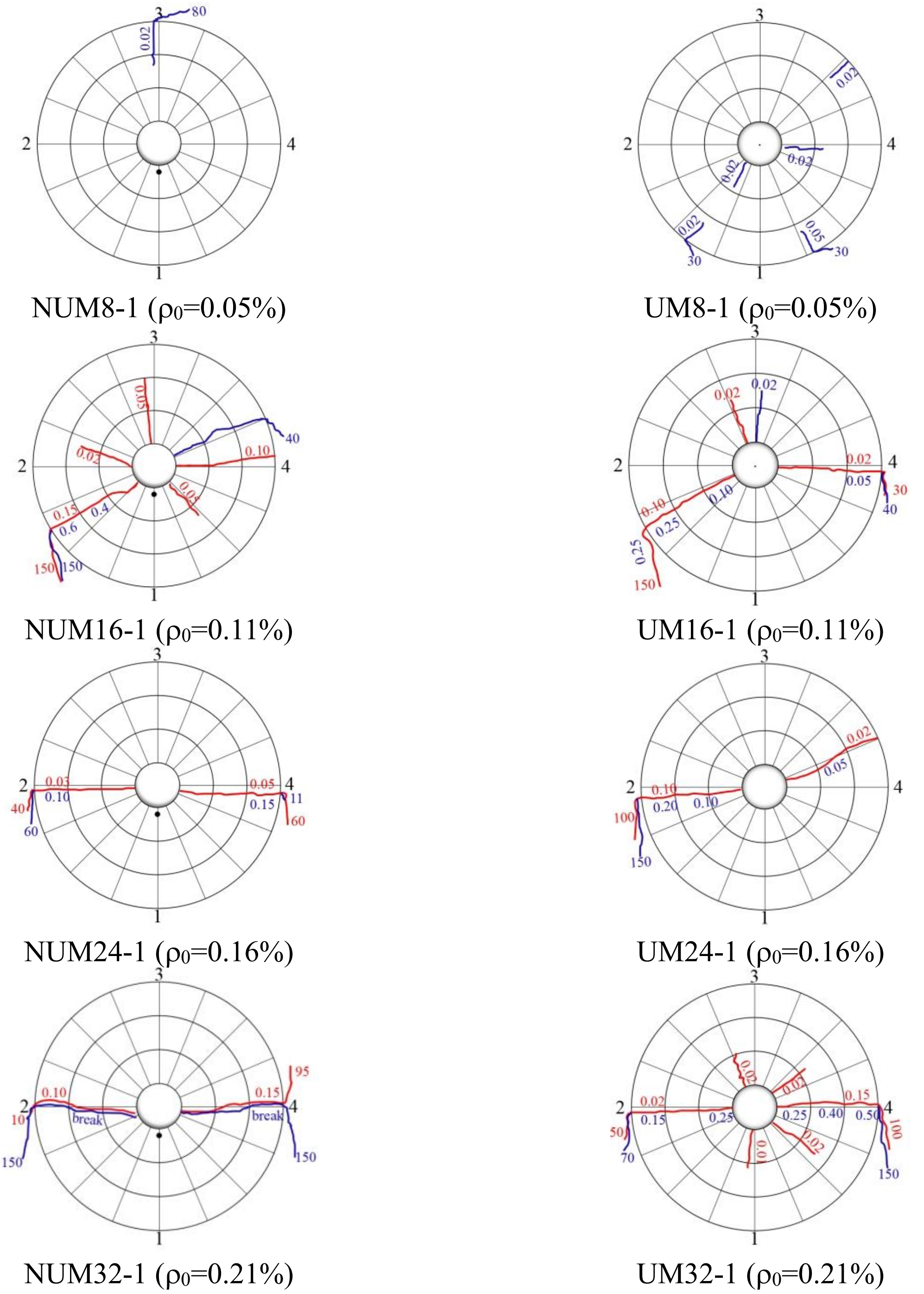

Fig. 11. Crack patterns in cement mortar specimens (NUM denotes non-uniform corrosion mortar sample, UM denotes uniform corrosion mortar sample).

4.3.2. Cracking profiles of ECC specimens

The cracking profiles of ECC specimens are presented in Fig. 12. No corrosion-induced crack was observed after 1d corrosion (ρ_0=0.16%). Some micro-cracks (~0.001 mm) were observed when the corrosion duration was increased to 2d (ρ_0=0.32%), but there was still no obvious corrosion-induced crack on the sample surface. When corrosion duration increased to 4d (ρ_0=0.64%), the NUECC specimens developed an average crack width of 0.04 mm, while the 6d (ρ_0=0.96%) NUECC specimens had an average crack width of 0.016 mm. The average crack width of UECC samples at 4d (ρ_0=0.64%) corrosion duration specimens was 0.024mm. When the corrosion duration increased to 6d (ρ_0=0.96%), the average crack width increased to 0.04mm. Most cracks of NUECC specimens were concentrated in 2 – 4 (or 90° – 270° line) direction, while the UECC specimens presented randomly distributed cracks, and this pattern was consistent with the observation of mortar samples. Statistical analysis of crack distributions is presented in the following section.

Fig. 12 shows that there were many micro-cracks (~0.001 mm) on the surface of ECC specimens. These micro-cracks released the expansion stress generated by the corrosion products. Thus, no corrosion cracks appeared in 1d and 2d corrosion ECC specimens, and 6d NUECC specimens' average crack width was even smaller than 4d's. The design corrosion rates of ECC specimens were pronouncedly higher than those of mortar specimens, but the crack width of ECC specimens was smaller than that of ECC specimens. This can be explained by the generation of those microcracks and the excellent tensile performance of ECC. The appearance of microcracks released the expansion stress generated by corrosion products. In addition, the high ductility of ECC can bear the volume expansion of corrosion products. Thus, compared with mortar specimens, the crack width of ECC specimens was significantly lower, even though the corrosion rates of ECC specimens were higher than those of mortar specimens.

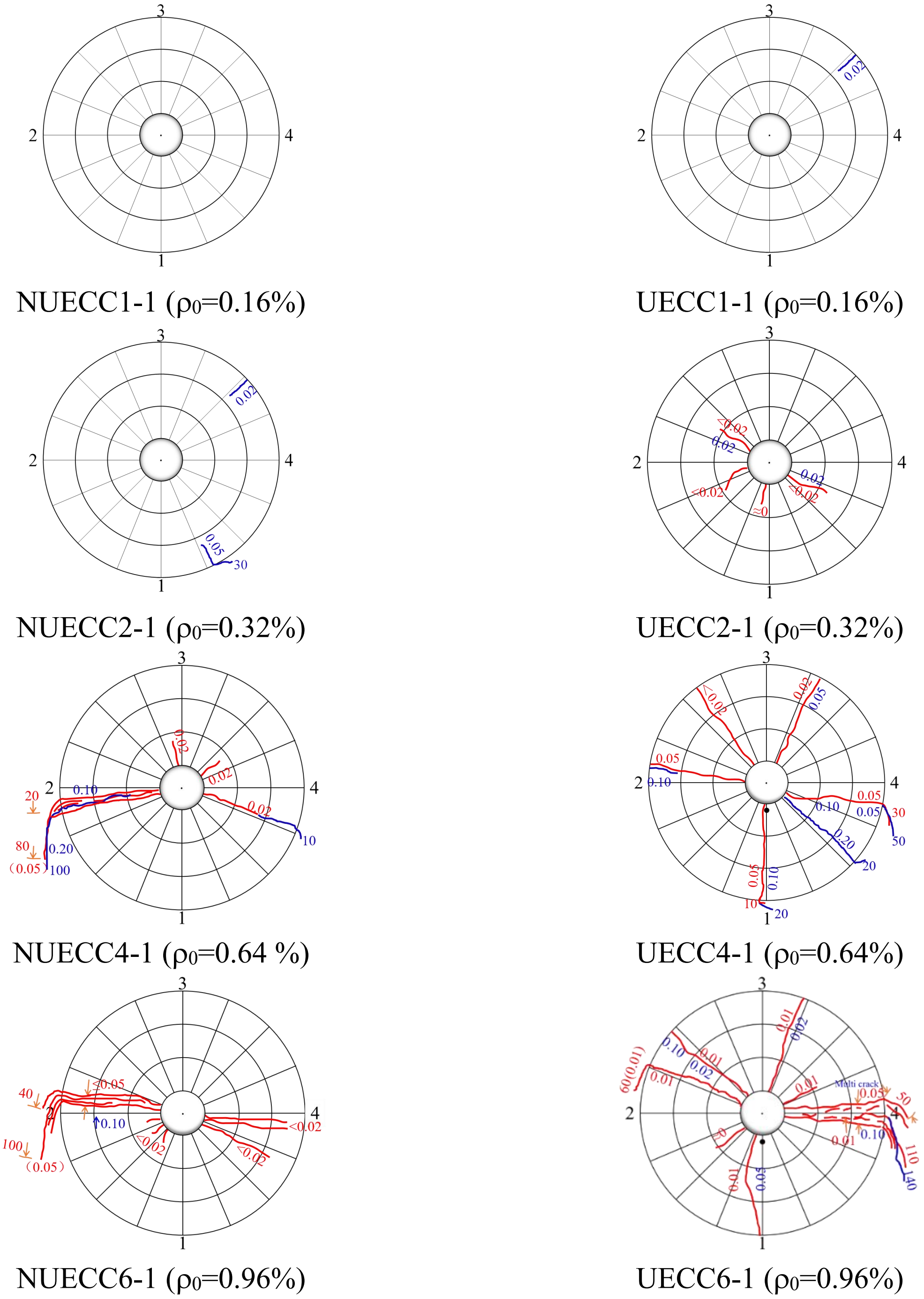

Fig. 12. Crack patterns in ECC specimens (NUECC denotes non-uniform corrosion ECC sample, UECC denotes uniform corrosion ECC sample).

4.3.3. Statistical analysis on cracking patterns of non-uniform and uniform corrosion cases

Fig. 13 illustrates the cracking patterns of cement mortar samples induced by corrosion and pull-out tests. In Fig. 13 (a) and (c), it is clear that most non-uniform corrosion (NU) induced cracks developed along the 90° – 270° line direction, while the uniform corrosion (U) induced cracks randomly distributed around the steel rebar. As discussed in section 4.2, in the case of non-uniform corrosion, most corrosion products accumulated in the side near the steel wire, while in the case of uniform corrosion, the corrosion products evenly distributed around the steel rebar. Consequently, the volume expansion of corrosion products from non-uniform corrosion generated non-uniform stress that was concentrated on the steel wire side, which further caused more cracks along the 90° – 270° line direction (or 2 – 4 line direction in Fig. 11). Nevertheless, products generated by uniform corrosion were evenly distributed around the steel rebar. Thus, compared with the concentrated stress in the case of non-uniform corrosion, the stress caused by the volume expansion of uniform corrosion products were uniformly distributed around the steel rebar. As such, with the same corrosion rate, the crack width of non-uniform corrosion was higher than that of uniform corrosion due to the concentrated stress.

The pull-out induced cracking patterns are presented in Fig. 13 (b) and (d). Compared with non-uniform corrosion, the pull-out cracks in uniform corrosion case distributed more uniformly around the steel rebar than that in non-uniform corrosion case. As presented in Fig. 11 and Fig. 12, most of pull-out cracks were induced along the corrosion cracks. Moreover, in non-uniform corrosion case, more corrosion pits were generated on the surface of steel rebar in the steel wire side, which in turn, increased the friction force between the steel rebar and mortar bulk in pull-out test. As a result, more pull-out induced cracks were observed on the side with the steel wire.

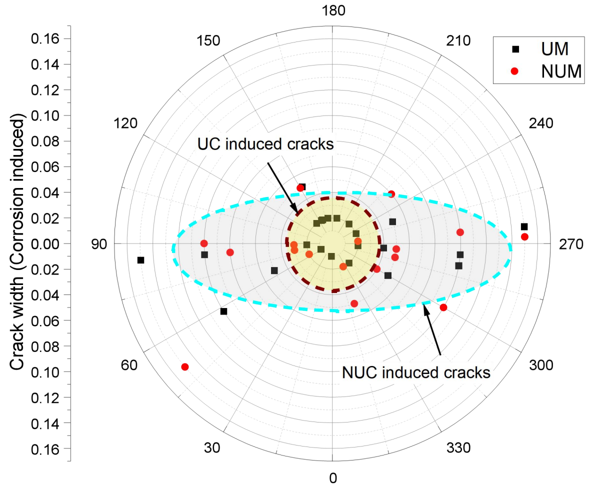

(a) Corrosion induced cracking patterns of mortar specimens.

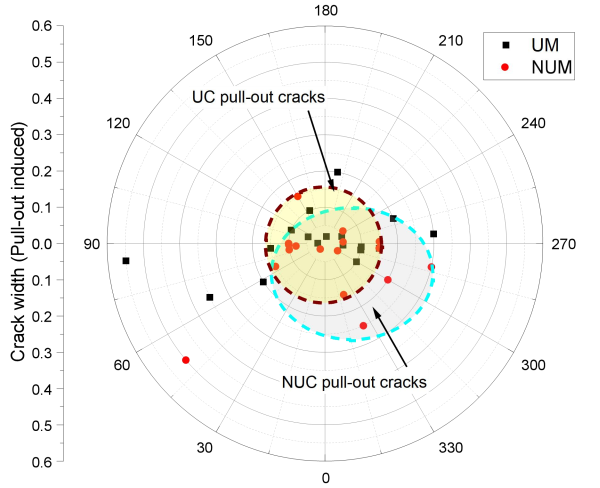

(b) Pull-out induced cracking patterns of mortar specimens.

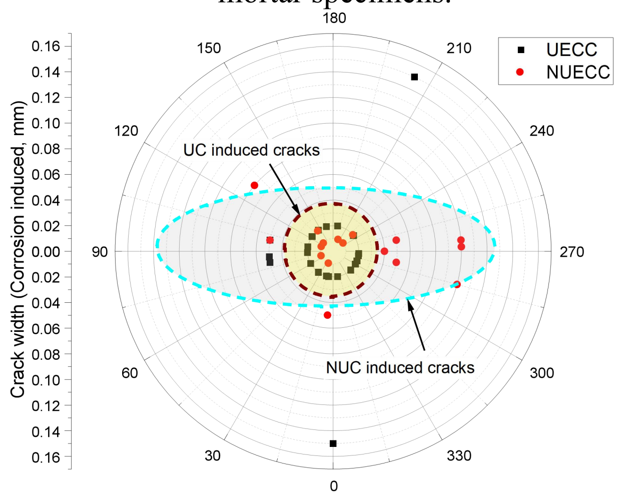

(c) Corrosion induced cracking patterns of ECC specimens.

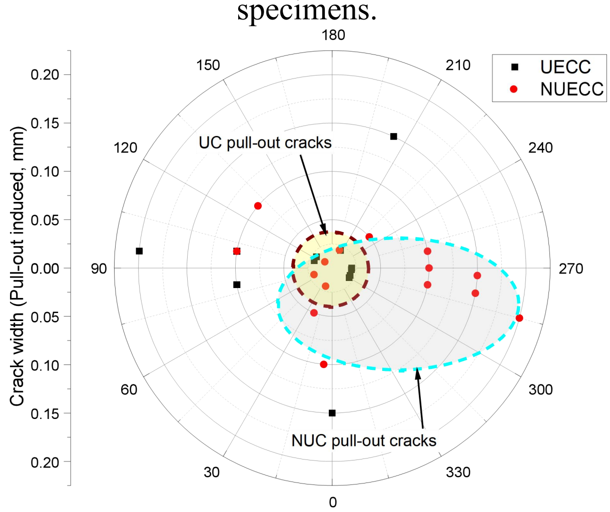

(d) Pull-out induced cracking patterns of ECC specimens.

Fig. 13. Cracking patterns of mortar and ECC specimens.

As discussed in previous sections, the corrosion induced cracks of non-uniform corrosion case were mostly concentrated alongside the 90° - 270° line direction, and the pull-out induced cracks of non-uniform corrosion case were distributed in the side with the steel wire, a similar cracking pattern for non-uniform corrosion case was also found in (Fu et al. 2021). Thus, as shown in Fig. 14, in order to count the corrosion induced crack distribution, the cross section of cylinder specimen was divided into 4 parts (i.e., part - A, B, C and D), and the cross section was divided into 2 parts (i.e., part I and II) to count the pull-out induced crack distribution.

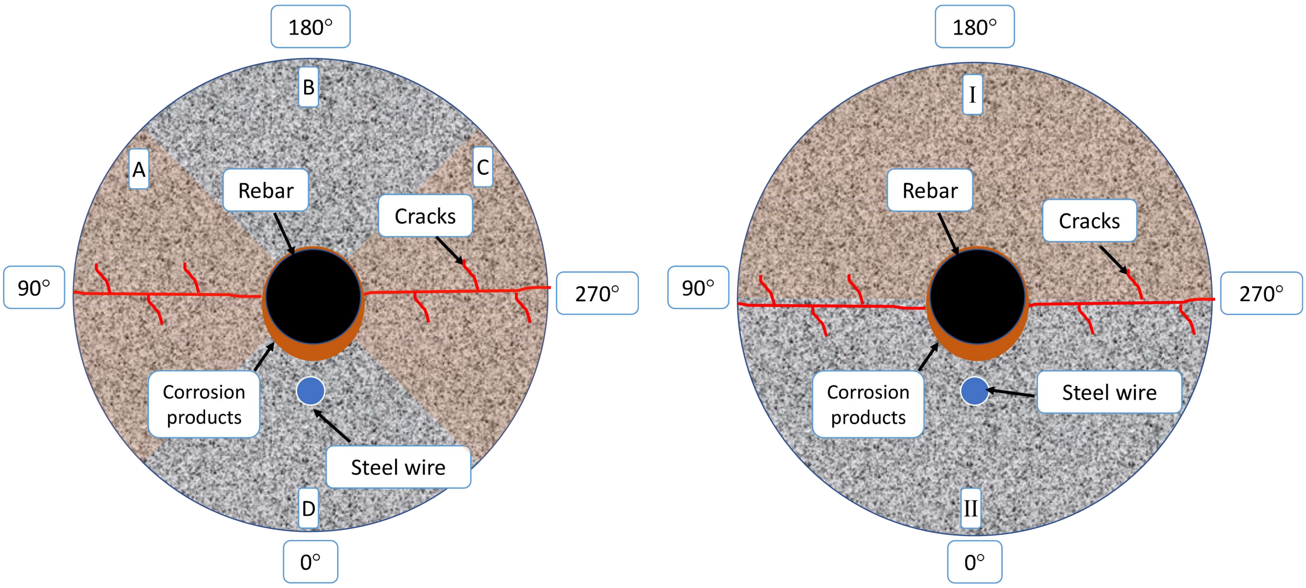

(a) Cross section was divided into 4 parts to count the corrosion induced cracks.

(b) Cross section was divided into 2 parts to count the pull-out induced cracks.

Fig. 14. Schematic of the cross-section division to statistically count the distribution of cracks.

Table 6 presents the average values of crack width as well as the possibilities of cracks in different parts induced by corrosion and pull-out tests. The crack width induced by non-uniform corrosion (i.e, NUM and NUECC) was significantly higher than uniform corrosion induced (i.e., UM and UECC), which corresponding with the previous discussion that the stress generated by the non-uniform corrosion products was more concentrated in one side. The pull-out induced crack widths for uniform corrosion and non-uniform corrosion cases did not show obvious difference. With the same corrosion method, the ECC matrix specimens showed lower crack width than the specimens with mortar as matrix even the design corrosion rate of most ECC specimens were higher than mortar specimens. The ECC material can restrain the development of the corrosion cracks in two aspects: (1) ECC can self-heal the micro-cracks, which can resist the transmission and diffusion of corrosive substances (i.e., chloride ions, water, oxygen), thereby the service life of the structure can be extended, (2) the randomly distributed fibers in the matrix, especially those distributed transversely to the steel bar, can continue to withstand tensile stress after the matrix cracks, effectively suppressing the propagation of longitudinal splitting cracks, and significantly improving the toughness of the matrix.

The non-uniform corrosion induced cracks (i.e., NUM and NUECC) have much higher possibility of appearing in parts A and C than that in parts B and D as shown in Fig. 14 (a), while the uniform corrosion induced cracks (i.e., UM and UECC) have similar possibility of appearance in parts A+C and parts B+D. This agrees with the illustration in Fig. 13 (a) and (c) that the cracks induced by non-uniform corrosion concentrated alongside the 90° - 270° line direction while the uniform corrosion induced cracks randomly distributed around the steel rebar.

The pull-out cracks for non-uniform cases (i.e., NUM and NUECC) also showed unevenly appearance possibilities in parts I and II as divided by Fig. 14 (b) method. In uniform corrosion cases (i.e., UM and UECC), the cracks uniformly distributed in these two parts, which is reasonable since most of the pull-out cracks developed alongside the corrosion cracks, and the uniform corrosion induced cracks were evenly distributed around the steel rebar as discussed previously. For non-uniform corrosion case, the unevenly distributed corrosion pits also increased the friction force on the side close to the steel wire (i.e., part I in Fig. 14) while the corrosion pits in uniform corrosion case were evenly distributed. Consequently, the possibilities of pull-out cracks in part I of non-uniform corrosion cases (i.e., NUECC and NUM) were higher than in part II.

4.4. Bonding performance analysis

Assuming that the bond stress is evenly distributed in the rebar-mortar/ECC interface, the ultimate rebar-mortar/ECC bond strength (τ_u) of a specimen can be determined by the ultimate pull-out load and the bonding surface area as expressed in Eq. :

$$\tau_u = \frac{T_u}{\pi d l} \tag{2}$$

where T_u represents the ultimate load in pull-out tests (N), d denotes the diameter of steel rebar in this work (mm) and l is the bonding length in this work (mm).

The results of corrosion rate, average bond strength and slip value at peak of all specimens are summarized in Table 7. The average bond stress of reference mortar (UM0) and ECC (UECC0) specimens were 2.47 MPa and 3.46 MPa, respectively. The bond stress of reference ECC specimens was 28.6% higher than the mortar samples. As discussed before, the tensile strength and the cracking resistance ability of ECC are higher than mortar. Thus, during the pull-out test, the generated microcracks were prevented to develop by fibers in ECC specimens while the mortar specimens had limited resistance to prevent the development of microcracks. Thus, the bond strength of UECC0 specimens was higher than UM0 specimens.

In Table 7, The bond strength of corroded specimen was 3-10 times higher than that of corresponding uncorroded specimen. The reason for the enhanced bond strength of corroded specimens can be attributed to the generation of mechanical bite force. For uncorroded specimens, the bond strength was mainly provided by the chemical bond force and friction force. There was limited mechanical bite force between round steel rebar and sample matrix. Nevertheless, after corrosion process, corrosion pits were generated on rebar surface, which significantly increased the friction force and mechanical bite force in between rebar and sample matrix. As a result, the corroded specimens had higher bond strengths than uncorroded specimens.

Given the cracking patterns of corroded ECC and mortar specimens showed significant difference as been discussed in previous sections. The bonding performance of corroded specimens is expected to be quite different between ECC and mortar specimens. In this section, the influence of corrosion methods and the bulk material types on bonding performance are discussed comprehensively.

(a) Pull-out failure (PO) (b) Splitting failure (SP)

Fig. 15. Different failure modes

4.4.1. Bond stress-slip behavior

The slip of steel rebar and mortar/ECC matrix can be calculated in accordance with Eq.

$$S_{av}=\frac{s_f+s_d}{2}-\varepsilon L \quad (3)$$

Where s_f is the slip between the free end of rebar and the sample matrix, s_d represents the slip between the loading end and the sample matrix, ε represent the measured tensile strain of the steel rebar and L is the length of the steel rebar between the loading end and the anchorage of MTS.

Typical bond stress-slip curves for NUM-24h and NUECC-1d specimens are presented in Fig. 16, both of the specimens had the same design corrosion rate (i.e., ρ_0=0.16%). The NUM-24h specimens showed splitting failure mode (i.e., Fig. 15 (b)) while the NUECC-1d specimen demonstrated a pull-out failure mode (i.e., Fig. 15 (a)) in pull-out tests. It can be observed in Fig. 16 NUM-24h specimen with splitting failure mode only had one slip section (OA_1), when it reached the ultimate load, specimen split rapidly since there was no other source could provide resistance to the sliding of steel rebar. Then, the bond stress reduced quickly, and the steel rebar was completely pulled out (i.e., A_1B_1 section). For specimens with pull-out failure mode, the stress-slip curve can be divided into 3 sections, including micro-slip section, failure section and residual section:

(1) Micro-slip section (OA_2): in this section, the chemical bond between reinforcement and ECC materials gradually break down. The fiber and mortar jointly bear the hoop tensile force. The cracked ECC specimens did not suddenly burst due to the presence of the fiber which could continue to bear the load until the ultimate load (bond strength). Due to the strong grip of the ECC material, the bond-slip curve developed linearly in this stage.

(2) Failure section (A_2B_2): when reached the peak stress, the mechanical bite force between the steel bar and the fiber mortar gradually decreased, the bond stress gradually decreased, and the interface slip significantly increased. In point B_2, the steel rebar started to be pulled out, then the bond stress started to linearly decrease.

(3) Residual section (B_2C_2): the whole steel bar was slowly pulled out, and the bond stress mainly depends on the sliding friction resistance between corroded steel rebar and the ECC matrix.

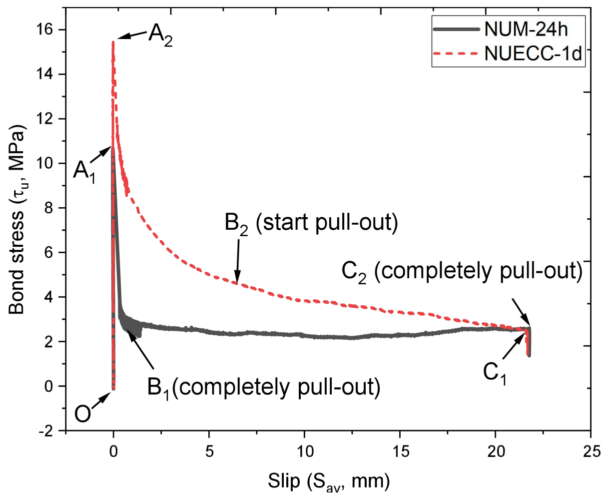

Fig. 16. Typical bond stress-slip curve.

4.4.2. Bond stress-slip performance of corroded specimens

The bond stress-slip curves of all mixtures are presented in Fig. 17. The slope of the ascending section of each curve was very close which indicates that the corrosion duration, corrosion methods, and the used of bulk materials have limited effect on the bonding stiffness of the specimens.

Compared with mortar specimens, ECC specimens showed better post-failure performance. In Fig. 17, the slip distance (i.e., A_2B_2 section in Fig. 16) for ECC specimens was longer than that of mortar specimens, which indicates that ECC materials have a better slip-resistance property after peak stress. When the steel rebar was pulled out (i.e., B_2C_2 section in Fig. 16), the stress-slip curves in Fig. 17 of mortar specimens developed horizontally while the ECC specimens still gradually decreasing, which implies the ECC materials can still provide sliding friction when steel rebar were pulling out. It can be seen from Table 7 that the failure modes of mortar samples are mostly splitting failure (SP) while ECC are mostly pull-out failure (PO). The SP failure mode denotes major cracks were observed during/after the pull-out tests. Thus, mortar samples could not provide any resistance after the generation of major cracks. On the other hand, the ECC samples kept intact during the pull-out tests, the ring stress was not completely released. As a result, the ring stress provides the friction force during the pull-out process for ECC samples. So, the post-failure performance of ECC is better than that of mortar specimens.

The residual bond stress for non-corrosion mortar sample was 1.45 MPa, while the non-uniform corrosion mortar specimens were 1.76-5.51 MPa and the uniform corrosion mortar specimens were 1.71-6.36 MPa. For ECC specimens, the residual bond stress of non-corrosion specimen was 1.95 MPa, the non-uniform corrosion ECC specimens were 7.59-12.94 MPa while the uniform corrosion specimens were 6.04-13.56 MPa. It can be seen that the residual bond stress for corroded specimens were higher than that of the non-corrosion samples. This can be concluded that the friction between the round rebar and mortar/ECC materials increased after corrosion, which increased its bonding performance.

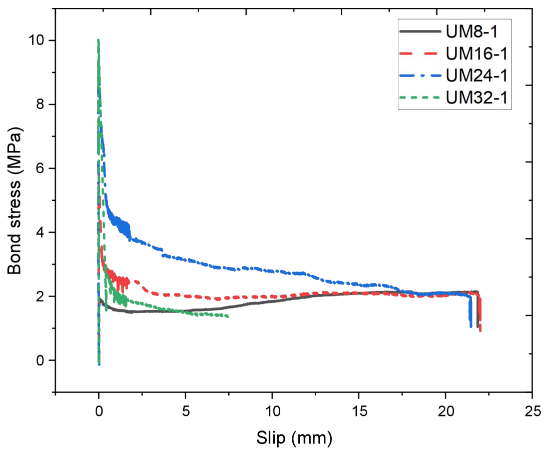

(a) Uniformly corroded mortar specimens.

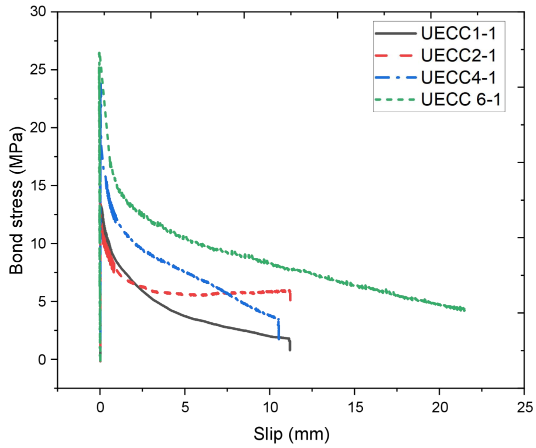

(b) Uniformly corroded ECC specimens

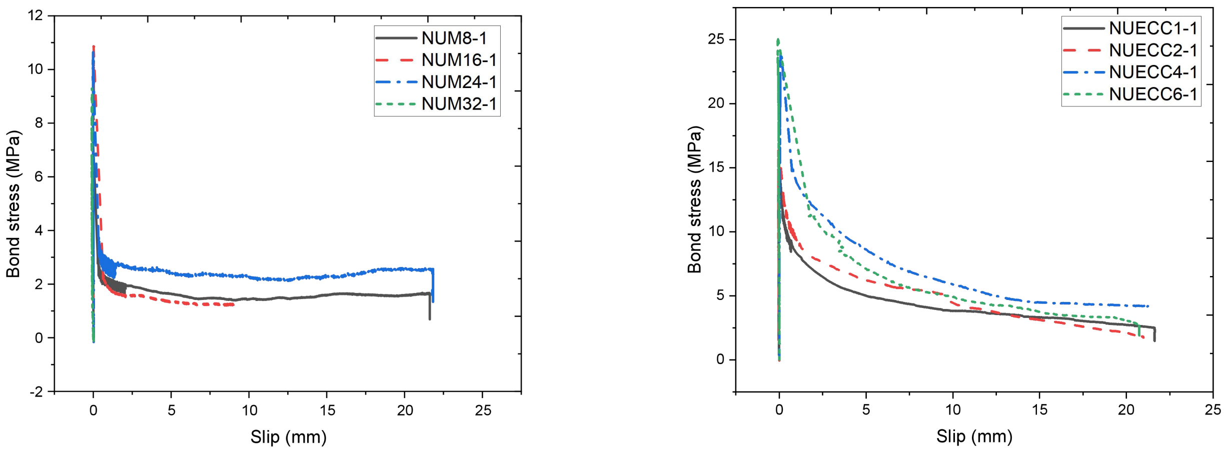

(c) Non-uniformly corroded mortar specimens (d) Non-uniformly corroded ECC specimens

Fig. 17. Bond stress-slip curves of all specimens.

4.4.3. Bond strength and corrosion rate relationship

Fig. 18 presents the bond strength of corroded specimens in terms of corrosion rate. It is found that the bond strength for ECC and mortar specimens is independent with corrosion method. Both mortar and ECC specimens showed a trend of increasing first and then decreasing with the development of corrosion rate. The increase trend of bond strength with corrosion rate indicates that the appearing of corrosion pits would generate bite force between steel rebar and cementitious matrix. However, the volume expansion of corrosion products generated cracks in matrix, and thus, the bite force would be released, and the bond strength decreased after a threshold corrosion rate value. The linear fitting results indicate that the threshold corrosion rate for mortar specimen is 0.125% while the ECC specimen has the threshold corrosion rate value of 0.922%. The excellent tensile strength and ductility of ECC material result in a much higher threshold corrosion rate value than mortar specimen.

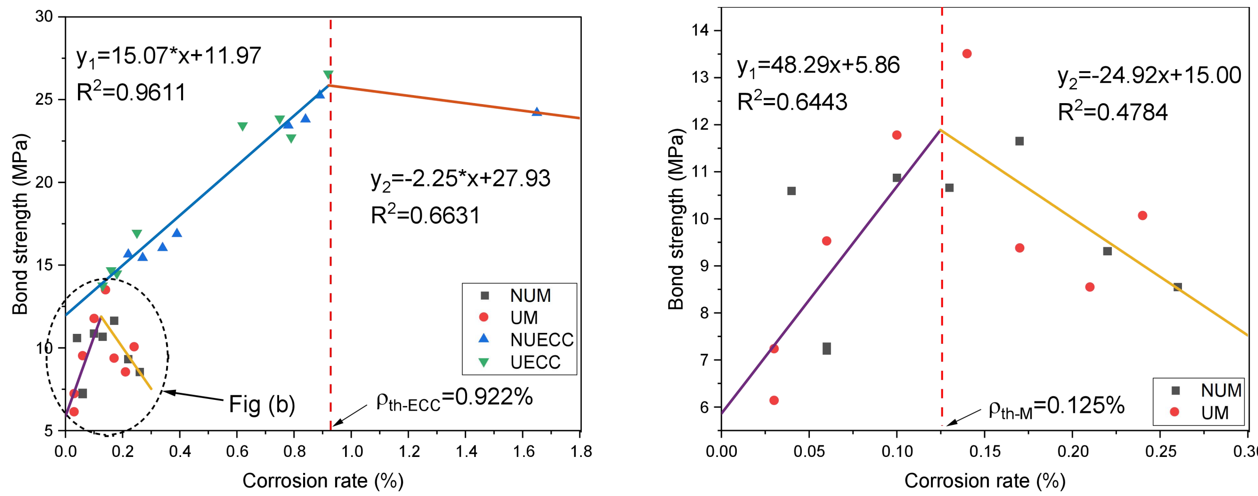

(a) ECC specimens (b) Mortar specimens

Fig. 18. Bond strength of corroded specimens in terms of corrosion rate.

5. Conclusions

In this work, the bonding performance of cement mortar and ECC materials under uniform and non-uniform corrosion methods were studied by electrical accelerated corrosion methods. The conclusions from this study can be drawn as follows:

1. Corrosion method has a great influence on cracking pattern. At a given corrosion level, the average crack width of mortar samples induced by non-uniform corrosion is generally larger than that induced by uniform corrosion, which can be attributed to the concentrated stress induced by the accumulated rust in non-uniform corrosion case. The micro-cracks generated in ECC specimens could release the expansion stress of rust. Thus, the average crack width of non-uniformly corroded ECC samples might be lower than that of uniformly corroded ECC samples (i.e., 6d of accelerated corrosion ECC samples in this work).

2. The uniform corrosion induced cracks evenly distributed around the steel rebar while the non-uniform corrosion induced cracks concentrated in a line perpendicular to the rebar -steel wire line which can be attributed to the rust accumulation.

3. Pull-out induced cracks developed along with the corrosion induced cracks. The pull-out cracks of uniform corroded specimens uniformly distributed around the specimen surface while the non-uniform corrosion specimens showed concentrated pull-out cracks on one side with more rust, which can be attributed to the corrosion pits which increased the friction and mechanical forces on the side close to the steel wire.
4. The bond strength of ECC and mortar specimens is independent with corrosion method. Both ECC and mortar specimens showed a trend of increasing first and then decreasing with the development of corrosion rate. The threshold corrosion rate for mortar specimen is 0.125% while the ECC specimen has the threshold corrosion rate value of 0.922%.

CRediT authorship contribution statement

Chuanqing Fu: Conceptualization, Methodology, Software, Visualization, Investigation. **Rui He:** Data curation, Writing- Original draft preparation, Writing- Reviewing and Editing. **Kejin Wang:** Supervision.

Data Availability Statement

Some or all data, models, or code that support the findings of this study are available from the corresponding author upon reasonable request.

Declaration of Competing Interest

The authors declare that they have no known competing financial interests or personal relationships that could have appeared to influence the work reported in this paper.

Acknowledgments

Most corrosion tests were performed during the time the first author visited Iowa State University (ISU), and the support from the Department of Civil, Construction and Environmental Engineering, ISU, on the experiments is greatly appreciated. Authors would also like to acknowledge the financial support from the Natural Science Foundation of Zhejiang Province (Grant No. LR21E080002, LZ20E080003), and the National Natural Science Foundation (Grant Nos. 51678529 and 51978620).

References

Abosrra, L., Ashour, A. F., and Youseffi, M. (2011). "Corrosion of steel reinforcement in concrete of different compressive strengths." *Construction and Building Materials*.

AL-mahmoud, F., Castel, A., François, R., and Tourneur, C. (2007). "Effect of surface pre-conditioning on bond of carbon fibre reinforced polymer rods to concrete." *Cement and Concrete Composites*, Elsevier, 29(9), 677–689.

ASTM C109 / C109M - 20b. (2020). *Standard Test Method for Compressive Strength of Hydraulic Cement Mortars (Using 2-in. or [50 mm] Cube Specimens)*. ASTM International, West Conshohocken, PA.

ASTM C150 / C150M-20. (2020). *Standard Specification for Portland Cement*. ASTM International, West Conshohocken, PA.

ASTM C618 - 19. (2019). *Standard Specification for Coal Fly Ash and Raw or Calcined Natural Pozzolan for Use in Concrete*. ASTM International, West Conshohocken, PA.

ASTM G1-03e1. (2017). *Standard Practice for Preparing, Cleaning, and Evaluating Corrosion Test Specimens*. ASTM International, West Conshohocken, PA.

ASTM G102-89(2015)e1. (2015). *Standard Practice for from Electrochemical Measurements*. ASTM International, West Conshohocken, PA.

BS EN 12504-3. (2005). *Testing concrete in structures - Part 3: Determination of pull-out force*. British Standards Institution.

Cao, C., and Cheung, M. M. S. (2014). "Non-uniform rust expansion for chloride-induced pitting corrosion in RC structures." *Construction and Building Materials*, Elsevier, 51, 75–81.

Coccia, S., Imperatore, S., and Rinaldi, Z. (2016). "Influence of corrosion on the bond strength of steel rebars in concrete." *Materials and Structures*, Springer Netherlands, 49(1–2), 537–551.

Dong, B., Fang, G., Liu, Y., Dong, P., Zhang, J., Xing, F., and Hong, S. (2017). "Monitoring reinforcement corrosion and corrosion-induced cracking by X-ray microcomputed tomography method." *Cement and Concrete Research*, Pergamon, 100, 311–321.

Du, P., Xu, D., Huang, S., and Cheng, X. (2017). "Assessment of corrosion of reinforcing steel bars in concrete using embedded piezoelectric transducers based on ultrasonic wave." *Construction and Building Materials*, Elsevier, 151, 925–930.

Fang, C., Lundgren, K., Plos, M., and Gylltoft, K. (2006). "Bond behaviour of corroded reinforcing steel bars in concrete." *Cement and Concrete Research*, Pergamon, 36(10), 1931–1938.

Fu, C., Fang, D., Ye, H., Huang, L., and Wang, J. (2021). "Bond degradation of non-uniformly corroded steel rebars in concrete." *Engineering Structures*, Elsevier Ltd, 226, 111392.

Fu, C., Jin, N., Ye, H., Jin, X., and Dai, W. (2017). "Corrosion characteristics of a 4-year naturally corroded reinforced concrete beam with load-induced transverse cracks." *Corrosion Science*, 117(1), 11–23.

Fu, C., Jin, N., Ye, H., Liu, J., and Jin, X. (2018). "Non-uniform corrosion of steel in mortar induced by impressed current method: An experimental and numerical investigation." *Construction and Building Materials*, Elsevier Ltd, 183, 429–438.

Fu, C., Li, S., He, R., Zhou, K., and Zhang, Y. (2022). "Chloride profile characterization by electron probe microanalysis, powder extraction and AgNO3 colorimetric: A comparative study." *Construction and Building Materials*, Elsevier Ltd, 341(May), 127892.

González, J. A., Miranda, J. M., and Feliu, S. (2004). "Considerations on reproducibility of potential and corrosion rate measurements in reinforced concrete." *Corrosion Science*, Pergamon, 46(10), 2467–2485.

He, R., Fu, C., Ma, H., Ye, H., and Jin, X. (2020). "Prediction of Effective Chloride Diffusivity of Cement Paste and Mortar from Microstructural Features." *Journal of Materials in Civil Engineering*, 32(8), 04020211.

He, R., Li, S., Fu, C., Zhou, K., and Dong, Z. (2022). "Influence of Cyclic Drying–Wetting and Carbonation on Oxygen Diffusivity of Cementitious Materials: Interpretation from the Perspective of Microstructure." *Journal of Materials in Civil Engineering*, 34(10), 04022256.

He, R., Ma, H., Hafiz, R. B., Fu, C., Jin, X., and He, J. (2018). "Determining porosity and pore network connectivity of cement-based materials by a modified non-contact electrical resistivity measurement: Experiment and theory." *Materials & Design*, Elsevier Ltd, 156, 82–92.

He, R., Ye, H., Ma, H., Fu, C., Jin, X., and Li, Z. (2019). "Correlating the Chloride Diffusion Coefficient and Pore Structure of Cement-Based Materials Using Modified Noncontact Electrical Resistivity Measurement." *Journal of Materials in Civil Engineering*, American Society of Civil Engineers, 31(3), 04019006.

Hong, S., Shi, G., Zheng, F., Liu, M., Hou, D., and Dong, B. (2020). "Characterization of the corrosion profiles of reinforcement with different impressed current densities by X-ray micro-computed tomography." *Cement and Concrete Composites*, Elsevier Ltd, 109(February), 103583.

Huang, C.-H. (2014). “Effects of Rust and Scale of Reinforcing Bars on the Bond Performance of Reinforcement Concrete.” *Journal of Materials in Civil Engineering*, 26(4), 576–581.

Ju, Y., Shen, T., and Wang, D. (2020). “Bonding behavior between reactive powder concrete and normal strength concrete.” *Construction and Building Materials*, Elsevier, 242, 118024.

Lee, H. S., Noguchi, T., and Tomosawa, F. (2002). “Evaluation of the bond properties between concrete and reinforcement as a function of the degree of reinforcement corrosion.” *Cement and Concrete Research*.

Li, C. Q., Yang, Y., and Melchers, R. E. (2008). “Prediction of reinforcement corrosion in concrete and its effects on concrete cracking and strength reduction.” *ACI Materials Journal*.

Li, F., and Yuan, Y. (2013). “Effects of corrosion on bond behavior between steel strand and concrete.” *Construction and Building Materials*.

Lim, Y. M., and Li, V. C. (1997). “Durable repair of aged infrastructures using trapping mechanism of engineered cementitious composites.” *Cement and Concrete Composites*, Elsevier Ltd, 19(4), 373–385.

Lin, H., Zhao, Y., Yang, J. Q., Feng, P., Ozbolt, J., and Ye, H. (2019). “Effects of the corrosion of main bar and stirrups on the bond behavior of reinforcing steel bar.” *Construction and Building Materials*.

Ling, Y., Wang, K., Li, W., Shi, G., and Lu, P. (2019). “Effect of slag on the mechanical properties and bond strength of fly ash-based engineered geopolymer composites.” *Composites Part B:*

Engineering, Elsevier Ltd, 164, 747–757.

Liu, W. S., Dai, G. L., and He, X. H. (2013). "Sensitive factors research for track-bridge interaction of Long-span X-style steel-box arch bridge on high-speed railway." *Journal of Central South University*, Springer, 20(11), 3314–3323.

Okada, K., Kobayashi, K., and Miyagawa, T. (1988). "INFLUENCE OF LONGITUDINAL CRACKING DUE TO REINFORCEMENT CORROSION ON CHARACTERISTICS OF REINFORCED CONCRETE MEMBERS." *ACI Structural Journal*.

Qiao, D., Nakamura, H., Yamamoto, Y., and Miura, T. (2016). "Crack patterns of concrete with a single rebar subjected to non-uniform and localized corrosion." *Construction and Building Materials*, Elsevier Ltd, 116, 366–377.

Stewart, M. G. (2009). "Mechanical behaviour of pitting corrosion of flexural and shear reinforcement and its effect on structural reliability of corroding RC beams." *Structural Safety*.

Yang, Y., Nakamura, H., Miura, T., and Yamamoto, Y. (2019). "Effect of corrosion-induced crack and corroded rebar shape on bond behavior." *Structural Concrete*, 20(6), 2171–2182.

Yu, J., Lin, J., Zhang, Z., and Li, V. C. (2015). "Mechanical performance of ECC with high-volume fly ash after sub-elevated temperatures." *Construction and Building Materials*, Elsevier, 99, 82–89.

Yu, K., Ding, Y., and Zhang, Y. X. (2020). "Size effects on tensile properties and compressive strength of engineered cementitious composites." *Cement and Concrete Composites*, Elsevier, 113, 103691.

Zhang, R., Castel, A., and François, R. (2009). "The corrosion pattern of reinforcement and its influence on serviceability of reinforced concrete members in chloride environment." *Cement and Concrete Research*, Pergamon, 39(11), 1077–1086.

Zhang, Z., and Zhang, Q. (2018). "Matrix tailoring of Engineered Cementitious Composites (ECC) with non-oil-coated, low tensile strength PVA fiber." *Construction and Building Materials*, Elsevier, 161, 420–431.

Zhu, W., Dai, J.-G., and Poon, C.-S. (2018a). "Prediction of the bond strength between non-uniformly corroded steel reinforcement and deteriorated concrete." *Construction and Building Materials*, 187, 1267–1276.

Zhu, W., François, R., Zhang, C., and Zhang, D. (2018b). "Propagation of corrosion-induced cracks of the RC beam exposed to marine environment under sustained load for a period of 26 years." *Cement and Concrete Research*, Pergamon, 103, 66–76.

Tables:

Table 1. Chemical compositions of Portland cement and fly ash used in this work.

Composition	SiO_2	Al_2O_3	Fe_2O_3	CaO	Na_2O	K_2O	MgO	SO_3	Other	LOI
Cement, %	19.2	5.29	2.48	63.69	0.04	0.51	2.88	2.82	0.39	2.7
Fly ash, %	30.7	16.48	6.8	28.8	2.97	0.27	6.74	3.47	3.28	0.49

Table 2. Physical properties of PVA fibers.

Length (L_f), mm	12
Diameter (D_f), µm	39
Aspect ratio (L_f/d_f)	308
Modulus of elasticity (E_f), GPa	42.8
Fiber strength, MPa	1600
Fiber density, g/cm^3	1.3
Surface-coated by Oil (by wt.)	1.2%

Table 3. Mixture proportion (by wt.)

Mixture ID	Binder (%)			FA/binder	SS/binder	Water/binder	SP/binder(%)	Volume of fiber
	Cement	FA	SS					
Mortar	0.2	0.8	0.2	0.8	0.2	0.22	0.60	0
ECC	0.2	0.8	0.2	0.8	0.2	0.22	0.60	2%

Table 4. A summary of cylinder specimens used in this work.

Sample ID	Test purposes	Materials	Corrosion types	Design corrosion rate (ρ_0,%)	Corrosion durations
UC	Corrosion uniformity test	ECC	Uniform (U)	/	5 d
NUC			Non-uniform (NU)	/	5 d
UECC0 (Ref)	Corrosion crack monitoring and	ECC	Uniform (U)	0	0 d
UECC1				0.16	1 d
UECC2				0.32	2 d
UECC4				0.64	4 d

UECC6	bonding strength tests			0.96	6 d
NUECC1			Non-uniform (NU)	0.16	1 d
NUECC2				0.32	2 d
NUECC4				0.64	4 d
NUECC6				0.96	6 d
UM0 (Ref)		Mortar	Uniform (U)	0	0 h
UM8				0.05	8 h
UM16				0.11	16 h
UM24				0.16	24 h
UM32				0.21	32 h
NUM8			Non-uniform (NU)	0.05	8 h
NUM16				0.11	16 h
NUM24				0.16	24 h
NUM32				0.21	32 h

Note: Each mixture for bonding strength tests has 2 duplicates.

Table 5. Parameters used for FEM simulation.

Parameter	Symbol	Value	Unit	Source
External current density	i	2	A/m^2	Controlled in tests
Anodic exchange current density	i_a^0	3×10^{-4}	A/m^2	(Cao and Cheung 2014)
Cathodic exchange current density	i_c^0	1×10^{-5}	A/m^2	
Andic equilibrium potential vs. SCE	φ_a^0	-0.78	V	
Cathodic equilibrium potential vs. SCE	φ_c^0	1.6	V	
Anodic Tafel slope	β_a	0.090	V/dec	
Cathode Tafel slope	β_c	-0.180	V/dec	
ECC resistivity	ρ	200	Ωm	
Volumetric expansion ratio of rust	a	2.35		(Liu et al. 2013)

Note: SCE denotes saturated calomel electrode.

Table 6. Average values of crack width and the possibilities of cracks in different parts.

Mixtures	Corrosion crack width (mm)	Pull-out crack width (mm)	Possibilities of corrosion cracks in different parts (%)		Possibilities of pull-out cracks in different parts (%)	
			Part A+C	Part B+D	Part I	Part II
NUM	0.0647	0.1472	82.35	17.65	73.68	26.32
NUECC	0.0424	0.0856	76.47	23.53	56.25	43.75
UM	0.0492	0.1550	58.33	41.67	50.00	50.00
UECC	0.0359	0.0700	54.55	45.45	50.00	50.00

Table 7. Summarized results of corrosion and pull-out tests.

Sample ID	ρ_{des}, %	ρ_m, %	$\rho_{a,m}$, %	τ_u, MPa	$\tau_{a,u}$, MPa	η_τ, %	Failure mode
UM0-1	-	-	-	2.86	2.47	-	PO
UM0-2		-	-	2.07			PO
NUM32-1	0.21%	0.22%	0.24%	9.31	8.93	3.62	SP
NUM32-2		0.26%		8.55			SP
NUM24-1	0.16%	0.13%	0.15%	10.66	11.16	4.52	SP
NUM24-2		0.17%		11.65			SP
NUM16-1	0.11%	0.10%	0.08%	10.87	9.04	3.66	SP
NUM16-2		0.06%		7.2			SP
NUM8-1	0.05%	0.06%	0.05%	7.28	8.94	3.62	PO/SP
NUM8-2		0.04%		10.59			SP
UM32-1	0.21%	0.24%	0.23%	10.07	9.31	3.77	SP
UM32-2		0.21%		8.55			SP
UM24-1	0.16%	0.17%	0.16%	9.38	11.45	4.64	SP
UM24-2		0.14%		13.51			SP
UM16-1	0.11%	0.10%	0.07%	11.78	8.96	3.63	SP
UM16-2		0.03%		6.14			SP
UM8-1	0.05%	0.03%	0.05%	7.24	8.39	3.4	SP
UM8-2		0.06%		9.53			PO/SP
UECC0-1	-	-	-	2.86	3.46	-	PO
UECC0-2		-		4.05			PO
NUECC6-1	0.96%	0.89%	1.27%	25.26	24.73	7.15	PO
NUECC6-2		1.65%		24.2			PO
NUECC4-1	0.64%	0.78%	0.81%	23.44	23.63	6.83	PO
NUECC4-2		0.84%		23.81			PO
NUECC2-1	0.32%	0.39%	0.37%	16.89	16.47	4.76	PO
NUECC2-1		0.34%		16.04			PO
NUECC1-1	0.16%	0.27%	0.25%	15.44	15.55	4.49	PO
NUECC1-2		0.22%		15.65			PO
UECC6-1	0.96%	0.92%	0.86%	26.57	24.64	7.12	PO/SP
UECC6-2		0.79%		22.71			PO
UECC4-1	0.64%	0.62%	0.69%	23.44	23.65	6.84	PO

UECC4-2		0.75%		23.85			PO
UECC2-1	0.16%	0.16%	0.21%	14.68	15.82	4.57	PO
UECC2-2		0.25%		16.95			PO
UECC1-1	0.32%	0.18%	0.16%	14.49	14.13	4.08	PO
UECC1-2		0.13%		13.76			PO

Note:1. ρ_{des} denotes the design corrosion rate, ρ_{m} represents the measured corrosion rate of each specimen and $\rho_{a,m}$ is the average corrosion rate of the duplicated specimens.

2. τ_{u} denotes the measured bond strength of each specimen and $\tau_{a,u}$ is the average bond strength of duplicated specimens.

3. η_{τ} denotes the bond strength ratio between the corroded specimen and that of corresponding uncorroded specimen.

4. failure mode: PO denotes the pull-out failure, after pull-out test, sample remained intact, no major crack was observed (i.e., Fig. 15 (a)). SP denotes the splitting failure, after pull-out test, major cracks was observed, sample split into several parts (i.e., Fig. 15 (b)). PO/SP denotes a failure mode in between pull-out failure and splitting failure, major cracks was observed while specimen kept intact.